Atmos. Meas. Tech. Discuss., 8, 4451–4488, 2015
www.atmos-meas-tech-discuss.net/8/4451/2015/
doi:10.5194/amtd-8-4451-2015

Atmospheric Measurement Techniques Discussions
Open Access

Uncertainties of satellite-derived surface skin temperatures in the polar oceans: MODIS, AIRS/AMSU, and AIRS only

H.-J. Kang[1], J.-M. Yoo[2], M.-J. Jeong[3], and Y.-I. Won[4]

[1]Department of Atmospheric Science and Engineering, Ewha Womans University, Seoul 120-750, Republic of Korea
[2]Department of Science Education, Ewha Womans University, Seoul 120-750, Republic of Korea
[3]Deptment of Atmospheric and Environmental Sciences, Gangneung-Wonju National University, Gangneung, Gangwondo 210-702, Republic of Korea
[4]Wyle/NASA GSFC Earth Science Data and Information System (ESDIS), Greenbelt, MD 20771, USA

Received: 11 February 2015 – Accepted: 8 April 2015 – Published: 4 May 2015

Correspondence to: J.-M. Yoo (yjm@ewha.ac.kr)

Published by Copernicus Publications on behalf of the European Geosciences Union.

Abstract

Uncertainties in the satellite-derived Surface Skin Temperature (SST) data in the polar oceans during two periods (16–24 April and 15–23 September) of 2003–2014 were investigated and the three datasets were intercompared as follows: MODerate Resolution Imaging Spectroradiometer Ice Surface Temperature (MODIS IST), the SST of the Atmospheric Infrared Sounder/Advanced Microwave Sounding Unit-A (AIRS/AMSU), and AIRS only. AIRS only algorithm was developed in preparation for the degradation of the AMSU-A. MODIS IST was systematically up to 1.65 K warmer at the sea ice boundary and up to 2.04 K colder in the polar sea ice regions of both the Arctic and Antarctic than that of the AIRS/AMSU. This difference in the results could have been caused by the surface classification method. The spatial correlation coefficient of the AIRS only to the AIRS/AMSU (0.992–0.999) method was greater than that of the MODIS IST to the AIRS/AMSU (0.968–0.994). The SST of the AIRS only compared to that of the AIRS/AMSU had a bias of 0.168 K with a RMSE of 0.590 K over the Northern Hemisphere high latitudes and a bias of −0.109 K with a RMSE of 0.852 K over the Southern Hemisphere high latitudes. There was a systematic disagreement between the AIRS retrievals at the boundary of the sea ice, because the AIRS only algorithm utilized a less accurate GCM forecast over the seasonally-varying frozen oceans than the microwave data. The three datasets (MODIS, AIRS/AMSU and AIRS only) showed significant warming rates ($2.3 \pm 1.7 \sim 2.8 \pm 1.9\,\mathrm{K\,decade^{-1}}$) in the northern high latitude regions (70–80° N) as expected from the ice-albedo feedback. The systematic temperature disagreement associated with surface type classification had an impact on the resulting temperature trends.

1 Introduction

The satellite observations of the polar oceans have been more challenging than those of non-frozen ocean and land, because it is more difficult to identify clouds over the

AMTD
8, 4451–4488, 2015

various surfaces (Tobin et al., 2006). The surface skin temperature (SST) is one of the most important climate variables that is related to the surface energy balance and the thermal state of the atmosphere (Jin et al., 1997). Compared to ground-based observations, satellite-observed SST data play a crucial role in climate study and model development by providing a uniform resolution data over the globe. The retrievals of AIRS data over the last decade have a significant contribution to various climate studies and model evaluations (Aumann et al., 2003; Tian et al., 2013; Yoo et al., 2013). AIRS retrievals have produced atmospheric temperature, moisture, and ozone profiles on a global scale by the AIRS method itself or together with other instruments (Liu at al., 2008). A lot of comparisons of the AIRS/AMSU data against data from numerical forecast model analysis fields, radiosondes, lidar, and retrievals from high-altitude aircraft have been used to assess the accuracy of the retrievals (Tobin et al., 2006; Susskind et al., 2014). The AIRS retrieval algorithm has been developed and validated gradually with clear sky and clear/cloudy conditions over a non-frozen ocean and then the non-polar land and polar cases (Tobin et al., 2006).

The AIRS instrument suite, with its microwave instrument, has an advantage of measuring the radiation penetrating through clouds and polar darkness, and has high spectral resolution and coarse spatial resolution (Dong et al., 2006). However, the AIRS only algorithm using only AIRS observations has been developed due to the degradation of the AMSU-A. Microwave and multispectral radiometers were used for global mapping of the sea ice extent and dynamics, while the visible, near-infrared, and infrared sensors could obtain details on the ice concentration, snow/ice albedo, thickness, and IST during clear-sky conditions (Hall et al., 2004; Scott et al., 2014). The MODIS on Aqua, used as infrared measurements, was influenced by water and cloud contamination, but had a higher spatial resolution (Dong et al., 2006). In order to remove the cloud effects in the MODIS IST algorithm, MODIS cloud mask products were used (Hall et al., 2004).

Since AIRS and MODIS were co-located on Aqua, they have often been used to make a synergistic algorithm and they have been compared to each other frequently (Li et al., 2005; Molnar and Susskind, 2005). Molnar and Susskind (2005) validated

AMTD
8, 4451–4488, 2015

the accuracy of the AIRS/AMSU cloud products using MODIS cloud analyses, which have a higher spatial resolution than that of AIRS. Knuteson et al. (2006) compared the MODIS Collection 4 (C4) with the AIRS Version 3 (V3) on the land surface temperature (LST) for the eastern half of the US, showing that the monthly differences were approximately 3 K. Lee et al. (2013) investigated the characteristics of the differences between the MODIS land surface skin temperature/sea surface temperature and the AIRS/AMSU surface skin temperature across the globe, and found that the MODIS C5 product was systematically lower by 1.7 K than the AIRS/AMSU V5 product over land in the 50° N–50° S regions, but it was higher by 0.5 K than the AIRS/AMSU product over ocean. Particularly in the sea ice regions, the MODIS annual averages were larger than the AIRS/AMSU values, due to the differential errors in ice/snow emissivity between the retrieval methods (or channels) for the two data products. The differences between the MODIS and AIRS methods were reduced when the MODIS IST and AIRS/AMSU surface skin temperatures were compared for 9 days. The possible reasons for this include the satellite local crossing time (LCT) difference between them in the high latitude regions, and the emissivity difference between microwave and infrared channels, but more comparison studies are necessary for a longer period to pin down the reasons of such skin temperature discrepancies between MODIS and AIRS/AMSU.

The primary purpose of this study was to investigate a relative degree of agreement (or disagreement) among different datasets using the MODIS IST C5, the SST of the AIRS/AMSU, and AIRS only V6. The second purpose of this paper was to analyze the temperature trend differences affected by the temperature differences among different data products. The datasets used in this study were described in Sect. 2. In Sect. 3, we compared the MODIS and AIRS only data with the AIRS/AMSU values. We also analyzed the temperature trends from the three satellite-based datasets in Sect. 4, and in the conclusion we summarized our study.

AMTD
8, 4451–4488, 2015

2 Data and methods

The Aqua satellite carrying the AIRS, AMSU and MODIS instruments was launched on 4 May 2002 with the Earth's Radiant Energy System (CERES), Humidity Sounder for Brazil (HSB) and the Advanced Microwave Scanning Radiometer-EOS (AMSR-E). It has far exceeded its designed life span of 6 years and has a chance of operating into the 2020s (http://aqua.nasa.gov/). The Aqua satellite orbits the earth every 98.8 min with an equatorial crossing time going north (ascending) at 1.30 p.m. LT (daytime) and going south (descending) at 1.30 a.m. (nighttime) in a sun-synchronous, near polar orbit with an inclination of 98.2° and an operational altitude of 705 km (Tian et al., 2013).

As shown in Table 1, we used the datasets of MODIS IST (e.g., Hall et al., 2006) and SSTs of AIRS/AMSU and AIRS only over the Northern Hemisphere during 16–24 April and over the Southern Hemisphere on 15–23 September from 2003 to 2014 in order to avoid the polar night when the visible channels of the MODIS did not operate (Hall et al., 2004). The sea surface temperature observed from infrared channels of satellites indicates the values at the skin of sea water, in contrast with the sea surface temperature measured from buoys, of which values represent the temperature of bulk water near the sea surfaces. The infrared sea SST was measured at depths of approximately 10 µm within the oceanic skin layer (~ 500 µm) at the water side of the air–sea interface where the conductive and diffusive heat transfer processes dominated (Emery et al., 2001; Donlon et al., 2002; Liou, 2002).

As an imaging spectroradiometer, the MODIS with 36 bands has retrieved various physical parameters such as aerosol optical thickness, land and water surface temperature, leaf area index, and snow cover, etc. (Barnes et al., 1998; Hall and Riggs, 2007). MODIS produced the "sea ice by reflectance" and "IST" in order to identify sea ice (Riggs et al., 1999). The "sea ice by reflectance" was determined by the Normalized Difference Snow Index (NDSI), and the reflectance of Band 1 (0.645 µm) and Band 2 (0.858 µm). The NDSI was calculated using Band 4 (0.555 µm) and Band 7 (2.130 µm).

AMTD
8, 4451–4488, 2015

IST is used as another method for identifying sea ice. The IST derived from the "split-window method" in Eq. (1), where bands 31 and 32 centered at approximately 11 and 12 µm, respectively. The method was applied in order to identify the ice when the IST was less than 271.5 K. The cutoff temperature between water and ice (271.5 K) may vary depending on the region and season. The IST is calculated as follows:

$$\mathrm{IST} = a + bT_{11} + c(T_{11} - T_{12}) + d\,[(T_{11} - T_{12})(\sec\theta - 1)] \quad (1)$$

where T_{11} is the brightness temperature (K) in 11 µm, T_{12} is the brightness temperature (K) in 12 µm, and θ is the scan angle from nadir. The difference between the T_{11} and the skin temperature from the LOWTRAN can be less than 3 K for a skin temperature between 230 and 260 K (Key et al., 1997). Since the value of T_{11} itself was a good estimate, coefficients a–d were defined for the following temperature ranges: $T_{11} < 240$ K, $240\,\mathrm{K} \le T_{11} \le 260$ K, and $260\,\mathrm{K} < T_{11}$ (Riggs et al., 2006). The IST algorithm was only applied to the polar ocean pixels that were determined to be clear by the MODS cloud mask using visible reflectance (Hall et al., 2004). The surface in the IST algorithm was assumed to be snow (Key et al., 1997). MODIS ISTs were provided as daily polar fields with a 4 by 4 km resolution.

The AIRS spectrometer is a high spectral resolution spectrometer with 2378 channels in the thermal infrared spectrum and 4 bands in the visible spectrum (Won, 2008). The AIRS and AMSU were coupled in order to play a role as an advanced sounding system under clear and cloudy conditions (Aumann et al., 2003). The AIRS/AMSU algorithm is independent of the GCM except for the surface pressure of the bottom boundary conditions (Molnar and Susskind, 2005). V6 is the most current retrieval algorithm since the launch of AIRS instrument, and detailed descriptions are given in Olsen (2013b). The primary products from AIRS suite include the atmospheric temperature-humidity profiles, ozone profiles, sea/land surface skin temperature (SST), and cloud related parameters such as the outgoing longwave radiation (OLR) (Susskind et al., 2011). In the AIRS/AMSU algorithm, the surface classification was conducted using the brightness temperature difference in 23 GHz (AMSU ch1) and 50 GHz (AMSU ch3).

AMTD
8, 4451–4488, 2015

The difference (brightness temperature at 23 GHz minus brightness temperature at 50 GHz) had a negative value on the sea ice and a positive value on the water (Grody et al., 1999; Hewison and English, 1999). Also, the brightness temperature difference between 23 GHz (AMSU ch1) and 31 GHz (AMSU ch2) could distinguish the age of the sea ice (Kongoli et al., 2008).

After the surface type classification from the AMSU retrieval, the initial state for atmospheric and surface parameters, cloud parameters and OLR was generated using the Neural Network methodology (Susskind et al., 2011, 2014). The methodology was used to approximate some functions between the input and output vectors by training (Gardner and Dorling, 1998). Next, the initial clear column radiances were generated, which were based on the initial state and the observed infrared radiances. The surface and atmospheric variables, including the surface skin temperature, were retrieved by updating the cloud cleared infrared radiance, iteratively. The cloud properties and outgoing longwave radiation were then retrieved, followed by the error estimates and quality control. In the AIRS only V6, shortwave window region 3.76–4.0 µm was used in order to derive the surface skin temperature and surface spectral emissivity (ε).

AMSU channels 4–5 had not been available since 2007 and 2010, respectively, due to radiometric noise. In preparation for the degradation of the other AMSU channels, the AIRS only algorithm was developed excluding the AMSU observations. The algorithm was similar to that of AIRS/AMSU, but it did not use the AMSU-A observations in any step of the physical retrieval process and the quality control methodology. Instead, the AIRS only algorithm used the NOAA Global Forecast System (GFS) for surface classification purposes (Olsen, 2013a).

We calculated the climatology and anomaly values from the yearly 9 day mean temperatures in a 1° by 1° grid for the 12 year period of Aqua satellite observations in order to estimate the temperature anomaly trends. The trends of the MODIS IST were derived only when the number of yearly data was at least 10 out of 12 entire years at each grid point. The trends of the AIRS/AMSU and AIRS only were derived only when the number of yearly datasets was 12, covering the entire years of the analysis at each

AMTD
8, 4451–4488, 2015

grid. The bootstrap method (Wilks, 1995) was used to calculate at a 95 % confidence interval. In the method, 10 000 linear temperature trends were generated by random sampling, allowing repetition of 10 000 yearly anomaly temperature datasets. Then, we estimated the 95 % confidence interval of 10 000 temperature trends.

3 Comparison of the satellite-derived surface skin temperatures

Figure 1a shows the spatial coverage and the averaged value of the MODIS IST over the Southern Hemisphere during 15–23 September of 2003–2014. In order to solve the spatial resolution mismatches, the original resolution of the MODIS data with a 4 km by 4 km grid (Fig. 1a) was re-gridded to a 1° by 1° grid in the case of MODIS data present over 50 % (Fig. 1b). A grid spacing of 1° corresponds to approximately 111 km on the equator. In the zonal averaged SST analysis, this 50 % criterion was used. During the same period, the spatial distributions of the climatological T_{skin} (AA_V6) and T_{skin} (AO_V6) were also shown in Fig. 1c and d, respectively. As expected, the MODIS and AIRS showed the spatial distribution of the climatological SST, warmer at the lower latitudes than the higher latitudes. The SST distributions over the Northern Hemisphere during 16–24 April of 2003–2014 have been shown in Kang and Yoo (2015).

Figure 2a displays the number of years when both T_{skin} (MODIS) and T_{skin} (AA_V6) are available at each grid point over the Southern Hemisphere. The maximum number was 12. The number near 60° S was smaller than that of the other regions because the MODIS IST algorithm only produced its data in the cloud-free pixels. Similar distributions by the clouds were shown in Fig. 2b and d for the same reason. The reduced number of observations near 60° S had a spatial distribution similar to that of the frontal cloud bands that were likely associated with the mid-/high-latitude depressions encircling the Antarctica (e.g., Jakob, 1999; Comiso and Stock, 2001; Lachlan-Cope, 2010; Boucher et al., 2013). Figure 2c shows the number of years when both T_{skin} (AO_V6) and T_{skin} (AA_V6) were available at each grid. Most of the grids had both T_{skin} (AO_V6) and T_{skin} (AA_V6) for a period of more than 10 years.

AMTD
8, 4451–4488, 2015

Figure 3a presents the spatial distribution of the temporal difference in a 1° × 1° grid between the climatological T_{skin} (MODIS) and T_{skin} (AA_V6) during 16–24 April of 2003–2014 over the Northern Hemisphere. In general, T_{skin} (MODIS) at 60–70° N was higher than the T_{skin} (AA_V6). T_{skin} (MODIS) was about 3 K higher than the T_{skin} (AA_V6) on the Hudson Bay and near Greenland, whereas it was ~ 2 K lower near the center of the Arctic Ocean. The relationship between the climatological T_{skin} (MODIS) and T_{skin} (AA_V6) was presented in the scatter diagrams (Fig. 3b). The scatter plot revealed a temperature interval which deviated from the simple linear line. The discontinuous shape appeared at the freezing point (~ 273 K) and the turning point (~ 260 K) in terms of T_{skin} (MODIS), changing the coefficient of the MODIS IST algorithm. In the interval, T_{skin} (MODIS) was systematically higher than the T_{skin} (AA_V6) in the 260–273 K range of T_{skin} (MODIS). The slope in the range was 0.85, lower than the slope for the whole regression line (0.97). There was a better agreement in the 240–260 K range, where the difference between the T_{11} and the SST in the LOWTRAN was less than 3 K (Key et al., 1997). The better agreement in the range greater than 280 K was also shown.

Figure 3b was the same as Fig. 3a except for T_{skin} (MODIS) vs. T_{skin} (AO_V6). The differences between the two datasets were very similar to those in Fig. 3a. However, T_{skin} (MODIS) was more than 4 K higher than T_{skin} (AO_V6) in some regions near the Greenland and the Barents Sea. The slope (0.93) in the 260–273 K range of T_{skin} (MODIS) also indicated a deviation from the total slope (0.98) in the scatter plot (Fig. 3d), similar to that in Fig. 3b. Figure 3e showed the difference between T_{skin} (AO_V6) to T_{skin} (AA_V6). Overall, the agreement was much better than the previous two cases (Fig. 3a and c), except for in the Greenland Sea, the Barents Sea, and the Okhotsk Sea. Both T_{skin} (AO_V6) and T_{skin} (AA_V6) agreed with each other (r = 0.999) well except for near the freezing point.

Figure 4 showed discrepancies among the three types of SST datasets over the Southern Hemisphere during 15–23 September of 2003–2014. It has been noted that there was a latitudinal band encircling Antarctica at 60–70° S, where T_{skin} (MODIS) was higher than both the T_{skin} (AA_V6) and T_{skin} (AO_V6) (Fig. 4a and c). The circular region

AMTD
8, 4451–4488, 2015

corresponded to the sea ice/water boundary which was expected to move seasonally. This implies a systematic difference between T_{skin} (MODIS) and T_{skin} (AA_V6) in the sea ice classification. The corresponding scatter plots also revealed a discontinuous (i.e., not linear) shape in the 260–273 K range of T_{skin} (MODIS) (Fig. 4b and d). The slopes in that range were 0.84–0.94, which were smaller than the slope (0.98) in the whole range. In addition, T_{skin} (MODIS) showed lower temperature values than T_{skin} (AA_V6) and T_{skin} (AO_V6) near the Antarctic peninsula, in the region from Weddell Sea to Ross Sea (Fig. 4a and c).

The comparison between two types of AIRS datasets also showed the circular pattern around Antarctica where T_{skin} (AO_V6) was lower by 1.5–5.6 K than T_{skin} (AA_V6) (Fig. 4e). The discrepancy near the sea ice/water boundary was clear, possibly due to the difference in the sea ice detection method between the two datasets. The uncertainty of the SST at the sea ice boundary was distinguished from the other regions. Both T_{skin} (AO_V6) and T_{skin} (AA_V6) were in good agreement, other than the sea ice/water boundary regions. The scatter pattern of the T_{skin} (AA_V6) vs. that of the T_{skin} (AO_V6) showed that the two datasets generally agreed with each other, but the disagreement near the freezing point again occurred indicating a cold bias of AIRS only with respect to AIRS/AMSU (Fig. 4f).

Figure 5 showed the interannual variation of the spatial distributions for T_{skin} (MODIS) minus T_{skin} (AA_V6) in the Southern Hemisphere from 15–23 September of 2003–2014. Although the 9 day composite values were used in each year, T_{skin} (MODIS) data did not exist in some areas. It was because the MODIS IST algorithm was valid only for cloud-free pixels. The systematic positive values at the boundary of the sea ice consistently occurred, while the negative ones occurred on some areas of the sea ice near Antarctica every year.

Figure 6 presented the interannual variation of the spatial distribution of T_{skin} (AO_V6) minus T_{skin} (AA_V6) for the study period. As already seen in Fig. 4e, the values of T_{skin} (AO_V6) compared to T_{skin} (AA_V6) show systematic negative values encircling Antarctica during the period. In addition, there were positive values over the sea-ice

AMTD
8, 4451–4488, 2015

prevailing areas inside the circle, with the location varying from year to year, which must be related to the difference in the surface type characterization.

Table 2 showed the statistics of bias, spatial correlation coefficient (r), and root mean square error (RMSE) obtained from the 12 year climatologies of 2003–2014 in order to analyze the systematic error among the three types of satellite-observed temperatures quantitatively. This analysis for each hemispheric vernal period has been performed over the two regions (35–90° N, 60–90° N) of the Northern Hemisphere during 16–24 April, and over the regions (40–90° S, 60–90° S) of the Southern Hemisphere during 15–23 September. The values in parentheses indicated the average obtained from the statistics for each year and their corresponding SDs. Based on the climatology values, the SST of the AIRS retrievals were comparable with respect to the T_{skin} (MODIS) (r = 0.959–0.994). T_{skin} (MODIS) tended to systematically overestimate the AIRS retrievals over the polar oceans (bias = 0.198–0.597 K). Hall et al. (2004) reported the accuracy of T_{skin} (MODIS) with the bias values of 1.2–1.3 K near the South Pole and the Arctic Ocean. The RMSE of 1.847 K for T_{skin} (MODIS) vs. the T_{skin} (AA_V6) over 60–90° S in our study was slightly higher than that in the study of Hall et al. (2004).

From the intercomparison of the three datasets, the bias (−0.109–0.597) and RMSE (0.590–2.173) over the high latitude belt (60–90° N and S) tended to be larger, and the correlation coefficients (r = 0.959–0.986) was smaller than those over 35–90° N and 40–90° S among the three comparisons (Table 2). This result indicated that there was more disagreement over the high latitudes than over other regions. The spatial correlation coefficient (0.992–0.999) between T_{skin} (AO_V6) and T_{skin} (AA_V6) was greater than those (0.968–0.994) between T_{skin} (MODIS) and T_{skin} (AA_V6). In the high latitudes T_{skin} (AO_V6) with respect to T_{skin} (AA_V6) had a positive bias of 0.168 K with a RMSE of 0.590 K in the Northern Hemisphere, but a bias of −0.109 K with a RMSE of 0.852 K in the Southern Hemisphere. The high correlations (r = 0.998–0.999) between the AIRS/AMSU and AIRS only (i.e., AIRS retrievals) over the 35–90° N and 40–90° S areas showed that the AIRS only can be a good alternative for the AIRS/AMSU, except for at the region of the sea ice boundary (r = 0.992 over the 60–90° S). The disagree-

AMTD
8, 4451–4488, 2015

ment between T_{skin} (AA_V6) and T_{skin} (AO_V6) at the region where the sea ice and water mixed appeared, because the AIRS only used less accurate GCM forecast data for surface classification over the potentially frozen oceans.

Figure 7 presented the zonal mean temperature difference among the three satellite-observed datasets in a $1^{\circ} \times 1^{\circ}$ grid over the Northern Hemisphere during 16–24 April of 2003–2014 and over the Southern Hemisphere during 15–23 September 2003–2014. The red, blue and green lines represent the zonally averaged annual values of T_{skin} (MODIS) minus T_{skin} (AA_V6), T_{skin} (MODIS) minus T_{skin} (AO_V6), and T_{skin} (AO_V6) minus T_{skin} (AA_V6), respectively. The climatological annual values have been calculated from the interannually-varying yearly data, shown in Fig. 8. The black dashed line, the difference between the original MODIS IST data (4 km × 4 km) and converted T_{skin} (MODIS) ($1^{\circ} \times 1^{\circ}$) indicated the possible error from the conversion of spatial resolution. The differences by the conversion over both hemispheres were within 0.3 and 0.5 K, respectively. The original T_{skin} (MODIS), converted T_{skin} (MODIS), T_{skin} (AA_V6), and T_{skin} (AO_V6) were chosen under the same condition in space and time, and each grid ($1^{\circ} \times 1^{\circ}$) of a degree latitudinal band.

It is hard to see the systematic difference over the Northern Hemisphere due to the sea ice detection because of the distribution of continent in Fig. 3a. However, Fig. 7 clearly showed that the difference among the T_{skin} (MODIS), T_{skin} (AA_V6), and T_{skin} (AO_V6) also existed over the Northern Hemisphere. Compared to T_{skin} (AA_V6), T_{skin} (MODIS) overestimated in 56–81° N and 54–69° S, while T_{skin} (MODIS) underestimated in the other latitudinal zone. It has been noted that the peak of the difference between T_{skin} (MODIS) and two AIRS datasets in the Northern Hemisphere high-latitude region took place in broader region than in the Southern Hemisphere. T_{skin} (MODIS) was up to 1.65 K higher than the AIRS datasets at the boundaries of the sea ice/water, whereas it was lower by up to 2.04 K over the sea ice region. The MODIS IST algorithm was optimized on the snow/ice surface type, and thus the underestimation of T_{skin} (MODIS) in the 35–54° N and 40–55° S may not be unexpected. In general, the overestimation

AMTD
8, 4451–4488, 2015

of T_{skin} (MODIS) to the AIRS retrievals occurred at the sea ice boundary and the underestimation occurred in the sea ice region that can be covered with snow/ice.

The color-coded lines in Fig. 8 interannually represent the differences in temperature among the three datasets for individual years. The thick black lines indicated the yearly difference averages. There existed a significant degree of interannual variation in the difference between T_{skin} (MODIS) and the two AIRS datasets (Fig. 8a and b). The variation was larger in 2009, 2010 and 2011 over the regions northward of 60° N and southward of 55° S where sea ice existed. Figure 8b shows a value of T_{skin} (MODIS) minus T_{skin} (AO_V6) that was similar to that in Fig. 8a. T_{skin} (MODIS) was lower than T_{skin} (AO_V6) at the ice surface, but higher than T_{skin} (AO_V6) at the boundary of the sea ice. Figure 8c showed the interannual variation of T_{skin} (AO_V6) minus T_{skin} (AA_V6). The interannual variation of the difference between the AIRS retrievals was much larger in the high latitude than in the mid-latitudes. The maximum difference of 1.56 K between the AIRS retrievals was found at 87–88° N in 2011.

There could be several reasons for the observed differences between T_{skin} (MODIS) and T_{skin} (AA_V6). The main one can be attributed to the difference in the channel used for the retrievals of the skin temperature. The AIRS/AMSU V6 only utilized shortwave window channels for the surface skin temperature, while the MODIS IST algorithm used the longwave window regions. The shortwave window could be mixed with the solar radiation during the daytime, but it was suitable for temperature sounding (Chahine, 1975, 1977; Susskind et al., 2014). The advantage of the longwave window was that its range corresponded to the peak of the infrared radiation emitted from the earth (Prakash, 2000). On the other hand, the longwave window radiation could be affected more by clouds. In order to avoid cloud contamination, the MODIS IST algorithm analyzed the pixel when the MODIS cloud mask was reported as clear sky (Hall et al., 2004). The MODIS cloud mask using visible reflectance had a high accuracy during the daytime, but a lower accuracy during the nighttime due to low illumination. As another reason for the temperature difference, Lee et al. (2013) suggested that there were substantial differences in LCT between MODIS and AIRS in the high latitude regions, since

AMTD
8, 4451–4488, 2015

the different scan angles of the two instruments resulted in different footprints, which could lead to the observed difference in temperature. However, we suggested that the surface type classification method could be the primary reason for the temperature difference between the MODIS-based and AIRS-based datasets. AIRS/AMSU SST was retrieved after the surface type was classified. On the other hand, the MODIS IST was calculated without the surface type classification step. Then, the MODIS algorithm categorized pixels being ice if IST was less than the cutoff temperature. MODIS IST was calculated on the snow, sea ice, and ocean, assuming the surface was snow (sea ice). The IST was utilized as a criterion for identifying the ice/water which might cause significant disagreement between the T_{skin} (MODIS) and T_{skin} (AA_V6) in the range of 260–273 K.

4 Comparison of the surface skin temperature trends from the MODIS and AIRS/AMSU

In order to further investigate the effects of the difference among the satellite-observed temperatures from different measurement techniques or algorithms on the temperature anomaly trend, we calculated the trend in some latitude belts, using the three satellite-observed temperature datasets at each grid during 16–24 April of 2003–2014 (in the Northern Hemisphere) and 15–23 September of 2003–2014. During this period, an unusually extensive surface melting event was observed in 2012 (Nghiem et al., 2012; Hall et al., 2013; Comiso and Hall, 2014).

Table 3 shows the temperature anomaly trend with a 95 % confidence level on the 10° latitude belt. We arranged the data of MODIS IST, AIRS/AMSU, and AIRS only under the same condition in space and time. The significant warming trend in 70–80° N was estimated in the following order: AIRS/AMSU (2.83 K decade^{-1}) > AIRS only (2.71 K decade^{-1}) > T_{skin} (MODIS) (2.30 K decade^{-1}). The warming (0.10 to 0.38 K decade^{-1}) at 40–50° N and 50–60° S, and the cooling (−0.08 to −1.94 K decade^{-1}) at 80–90° N, 60–70° N, 50–60° N, 60–70° S, and 70–80° S,

AMTD
8, 4451–4488, 2015

of the three datasets occurred, but the trends were not significant. Comiso and Hall (2014) reported the SST trend using the Goddard Institute for Space Studies (GISS) dataset as 0.60 K decade^{-1} and the trend using the Advanced Very High Resolution Radiometer (AVHRR) dataset as 0.69 K decade^{-1} in the Arctic (> 64° N) during 1981–2012. Our result in 70–80° N, compared with the above studies, seems to indicate an acceleration in the Arctic warming.

The warming trend in the northern hemispheric high latitudes had been known to be caused in part by the well-known positive feedback among snow/ice, surface albedo and temperature (Curry et al., 1995; Comiso and Hall, 2014). T_{skin} (MODIS) had a greater cooling tendency compared to T_{skin} (AA_V6) in the higher latitude regions (70–90° N and 60–80° S) (Table 3). The trend difference between the two temperatures was −0.69 K decade^{-1} at 70–80° S. The trend difference of the T_{skin} (AA_V6) and T_{skin} (AO_V6) (i.e., AIRS only minus AIRS/AMSU) was the largest (−0.26 K decade^{-1}) at 60–70° N. The cooling trend (−0.90 K decade^{-1}) of the T_{skin} (AO_V6) was greater than that (−0.65 K decade^{-1}) of T_{skin} (AA_V6) at the latitude band.

Figure 9a and b showed the SST anomaly trends from the T_{skin} (MODIS) in a 1° by 1° grid over the Northern Hemisphere during 16–24 April of 2003–2014 and over the Southern Hemisphere during 15–23 September of 2003–2014. The T_{skin} (MODIS) trend was calculated on the grid, which had available data that existed for over 10 years. Figure 9c and d and Fig. 9e and f showed the trend data for T_{skin} (AA_V6) and T_{skin} (AO_V6), respectively, which all had 12 year data, individually. The trend distributions in all three of the datasets were similar over the Northern Hemisphere. Warming trend in the Beaufort Sea, East Siberian Sea and Kara Sea was detected, while cooling was observed in the Hudson Bay and near Greenland. The significant warming trend appeared at 70–80° N as shown in Table 3, and the trend based on the spatial distribution varied depending on the regions (Fig. 9a, c and e). According to Comiso and Hall (2014), a strong warming trend (> 1.5 K decade^{-1}) existed near the Kara Sea and Baffin Bay among the entire Arctic, consistent with the noticeable trend revealed near the Kara Sea in our study. Over the Southern Hemisphere, there were not enough data to

AMTD
8, 4451–4488, 2015

derive a trend for T_{skin} (MODIS) mostly due to clouds. The trend analysis over the sea ice regions from T_{skin} (AA_V6) and T_{skin} (AO_V6) showed a strong cooling trend, especially near the Antarctic peninsula between the Weddell and Ross Seas (Fig. 9d and f). The cooling trend was generally dominant over the Southern Hemisphere. Marshall et al. (2015) suggested that based on the model experiments, the cooling trend around Antarctica as opposed to the warming trend around the Arctic Ocean was the result of the offset between the greenhouse gas and ozone hole responses, emphasizing the larger cooling effects associated with the Antarctic ozone hole.

The 12 year mean of the T_{skin} (MODIS) minus T_{skin} (AA_V6) (Fig. 10a and c) and of the trend difference between T_{skin} (MODIS) and T_{skin} (AA_V6) (Fig. 10b and d) were compared in order to reveal the relationship between the temperature difference and the corresponding trend difference over the Northern Hemisphere during 16–24 April of 2003–2014 and over the Southern Hemisphere during 15–23 September of 2003–2014. T_{skin} (MODIS) was higher than T_{skin} (AA_V6) over the bays of Hudson and Baffin, and Bering Sea (Fig. 10a). The warming trend of the T_{skin} (MODIS) was also greater than that of the T_{skin} (AA_V6) over the Hudson Bay and near the Kara Sea (Fig. 10b). The data for the trend difference in the Southern Hemisphere was not sufficient due to the missing data of T_{skin} (MODIS) in the cloudy condition (Fig. 10d).

Figure 11 showed over both hemispheres the 12 year mean of the T_{skin} (AO_V6) minus T_{skin} (AA_V6) (Fig. 11a and c) and the corresponding trend difference of the T_{skin} (AO_V6) and T_{skin} (AA_V6) (Fig. 11b and d). The relationship of the temperature difference and trend difference over the Southern Hemisphere in Fig. 10 was hard to analyze due to the absence of a T_{skin} (MODIS) trend (Fig. 10c and d). However, Fig. 11c and d clearly showed that the temperature difference had a significant impact on the trend difference over the Southern Hemisphere. The trend of the T_{skin} (AA_V6) and T_{skin} (AO_V6) agreed well except for at the region of the sea ice boundary, implying that the algorithm identifying the sea ice affected the SST trend.

Table 4 quantitatively showed how the temperature differences among the three types of SST affected each trend difference over the hemispheric regions poleward

AMTD
8, 4451–4488, 2015

either from 50° N (shown in the left side of the table) during 16–24 April of 2003–2014 or from 50° S during 15–23 September of 2003–2014. In the upper portion, the average of the temperature difference and the trend difference in the grid corresponding to the temperature difference condition was used, whereas the average values on the grids that had the same signs for the temperature difference and the trend difference were used in the lower portion. Only the cases where grid number was greater than 100 were considered. The warmer temperature led to relatively warming trend, the cooler temperature led to relatively cooling trend. When the T_{skin} (MODIS) was greater than T_{skin} (AA_V6) in the regions poleward from 50° S, the trend difference was in the reduced cooling trend (i.e., warmer direction) as −0.96, −0.66, and −0.21 K decade^{-1} with the conditions of T_{skin} (MODIS) minus T_{skin} (AA_V6) rising as more than 1, 1.5 K, and 2 K, respectively. The uncertainty of the satellite-derived temperatures had a substantial effect on the uncertainty of the temperature trends.

5 Conclusions

The satellite-derived L3 products of MODIS IST and two SSTs from AIRS/AMSU and AIRS only were investigated with a comparative analysis during the vernal periods of 2003–2014: 16–24 April over the Northern Hemisphere and 15–23 September over the Southern Hemisphere. The original MODIS IST data were regridded onto a 1° × 1° grid box for comparison with the AIRS retrievals. The difference between the original MODIS IST and the converted one was within 0.5 K in a latitudinal belt.

The differences among the three types of satellite derived SST data were most prominent over the sea ice regions. T_{skin} (MODIS) and T_{skin} (AA_V6) were comparable (r = 0.97–0.99), but there existed systematic disagreement occurred in the T_{skin} (MODIS) range of 260–273 K. The southern hemispheric high latitude (60–90° S) was the primary contributor to the disagreement between them. In comparison with the T_{skin} (AA_V6) in a latitudinal belt, the T_{skin} (MODIS) was higher by up to 1.65 K than on the

AMTD
8, 4451–4488, 2015

boundary of the sea ice/water, whereas it was lower by up to 2.04 K in the sea ice region.

The spatial correlation coefficient (0.992–0.999) of the T_{skin} (AO_V6) and T_{skin} (AA_V6) was greater than that (0.968–0.994) between T_{skin} (MODIS) and T_{skin} (AA_V6). The T_{skin} (AO_V6) compared to the T_{skin} (AA_V6) had a bias of 0.168 K with a RMSE of 0.590 K over the Northern Hemisphere high latitudes and a bias of −0.109 K with a RMSE of 0.852 K over the southern hemispheric high latitudes. There was a systematic disagreement between the T_{skin} (AA_V6) and T_{skin} (AO_V6) at the sea ice boundary. It is likely due to the fact that the AIRS only algorithm utilized a less accurate GCM forecast than the microwave data over the seasonally-varying frozen oceans.

The temperature differences among the three types of datasets showed a high degree of interannual variations over the latitudinal belts where sea ice existed. The significant warming rates ($2.3 \pm 1.7 \sim 2.8 \pm 1.9\,\mathrm{K\,decade^{-1}}$) were revealed by all three datasets in the northern hemispheric high-latitude regions (70–80° N) could be interpreted as the ice-albedo feedback. The discrepancies between the trends of the T_{skin} (AA_V6) and T_{skin} (AO_V6) occurred at the sea ice boundary. When the T_{skin} (AA_V6) trends were compared to those of the T_{skin} (MODIS) or T_{skin} (AO_V6) in a 1° × 1° grid, the warmer temperature difference tended to lead to a relative warming trend, whereas the cooler temperature difference tended to lead to a relative cooling trend.

The systematic disagreement between the T_{skin} (MODIS) and T_{skin} (AA_V6) could be caused by (1) the channels used for the surface skin temperature, (2) the cloud contamination, (3) the LCT difference between the MODIS and AIRS, and (4) the surface type classification method. Whereas the AIRS/AMSU V6 used only the shortwave window channels for the surface skin temperature, MODIS IST used the longwave window regions. The MODIS IST product utilized the MODIS cloud mask with visible reflectance, which had lower accuracy during the night (Hall et al., 2004). Lee et al. (2013) reported that the LCTs between the MODIS and AIRS were almost the same from 60° N–60° S, but they were quite different in the high latitude regions. It is likely that the main cause

AMTD
8, 4451–4488, 2015

to the observed SST differences near the sea ice boundary was in the way the surface type was classified. The AIRS/AMSU algorithm conjugated the emissivity difference in the low and high frequency microwave bands (23 and 50 GHz) in order to identify sea ice. However, MODIS IST was calculated without the surface type classification.

The SST in the polar region is a useful parameter being used to derive the climate change signal, although it has been challenging to measure an accurate SST. Based on our results from detailed comparative investigation, we cautiously suggested that the observed difference and uncertainty among the satellite-derived SSTs were likely caused by the different sea ice detecting methods used in each algorithm. In addition, the methods also affected the temperature trend. In this study, we aimed to help in understanding characteristics of the infrared and microwave measurements for the surface skin temperature, and the method for identifying sea ice. We believe the results of this study can be useful for the interpretation and the modeling of the climate change associated with the temperature trends.

Acknowledgements. This study was supported by the National Research Foundation of Korea (NRF) grant funded by the Korean Government (MSIP) (No. 2009-0083527) and the Korean Ministry of Environment as the Eco-technopia 21 project (No. 201200016003).

References

Aumann, H. H., Chahine, M. T., Gautier, C., Goldberg, M. D., Kalnay, E., McMillin, L. M., Revercomb, H., Rosenkranz, P. W., Smith, W. L., Staelin, D. H., Strow, L. L., and Susskind, J.: AIRS/AMSU/HSB on the Aqua mission: design, science objectives, data products, and processing systems, IEEE T. Geosci. Remote, 41, 253–264, doi:10.1109/tgrs.2002.808356, 2003.

Barnes, W. L., Pagano, T. S., and Salomonson, V. V.: Prelaunch characteristics of the moderate resolution imaging spectroradiometer (MODIS) on EOS-AM1, IEEE T. Geosci. Remote, 36, 1088–1100, doi:10.1109/36.700993, 1998.

Boucher, O., Randall, D., Artaxo, P., Bretherton, C., Feingold, G., Forster, P., Kerminen, V.-M., Kondo, Y., Liao, H., Lohmann, U., Rasch, P., Satheesh, S. K., Sherwood, S., Stevens, B., and

AMTD
8, 4451–4488, 2015

Zhang, X. Y.: Clouds and aerosols, in: Climate Change 2013: The Physical Science Basis, Contribution of working group I to the fifth assessment report of the intergovernmental panel on climate change, Cambridge University Press, Cambridge, UK, 2013.
Chahine, M. T.: Remote sounding of cloudy atmospheres. I, the single cloud layer, J. Atmos. Sci., 31, 233–243, doi:10.1175/1520-0469(1974)031<0233:RSOCAI>2.0.CO;2, 1974.
Chahine, M. T.: Remote sounding of cloudy atmospheres, II, multiple cloud formations, J. Atmos. Sci., 34, 744–757, doi:10.1175/1520-0469(1977)034<0744:RSOCAI>2.0.CO;2, 1977.
Comiso, J. C. and Hall, D. K.: Climate trends in the Arctic as observed from space, Wiley Interdiscip. Rev.-Clim. Chang., 5, 389–409, doi:10.1002/wcc.277, 2014.
Comiso, J. C. and Stock, L. V.: Studies of Antarctic cloud cover variability from 1982 through 1999, Geoscience and Remote Sensing Symposium, 2001, IGARSS '01, IEEE 2001 International, 1782–1785, 2001.
Curry, J. A., Schramm, J. L., and Ebert, E. E.: Sea ice–albedo climate feedback mechanism, J. Climate, 8, 240–247, doi:10.1175/1520-0442(1995)008<0240:SIACFM>2.0.CO;2, 1995.
Dong, S. F., Gille, S. T., Sprintall, J., and Gentemann, C.: Validation of the Advanced Microwave Scanning Radiometer for the Earth Observing System (AMSR-E) sea surface temperature in the southern ocean, J. Geophys. Res.-Oceans, 111, 16, doi:10.1029/2005jc002934, 2006.
Donlon, C. J., Minnett, P. J., Gentemann, C., Nightingale, T. J., Barton, I. J., Ward, B., and Murray, M. J.: Toward improved validation of satellite sea surface skin temperature measurements for climate research, J. Climate, 15, 353–369, doi:10.1175/1520-0442(2002)015<0353:tivoss>2.0.co;2, 2002.
Emery, W. J., Castro, S., Wick, G. A., Schluessel, P., and Donlon, C.: Estimating sea surface temperature from infrared satellite and in situ temperature data, B. Am. Meteorol. Soc., 82, 2773–2785, doi:10.1175/1520-0477(2001)082<2773:esstfi>2.3.co;2, 2001.
Gardner, M. W. and Dorling, S. R.: Artificial neural networks (the multilayer perceptron) – a review of applications in the atmospheric sciences, Atmos. Environ., 32, 2627–2636, doi:10.1016/s1352-2310(97)00447-0, 1998.
Grody, N., Weng, F., and Ferraro, R.: Application of AMSU for obtaining water vapor, cloud liquid water, precipitation, snow cover and sea ice concentration, in: Technical proceedings of the tenth international atovs study conference, Colorado, USA, 27 January–2 February 1999, 230–240, 1999.
Hall, D. K. and Riggs, G. A.: Accuracy assessment of the MODIS snow products, Hydrol. Process., 21, 1534–1547, doi:10.1002/hyp.6715, 2007.

AMTD
8, 4451–4488, 2015

Hall, D. K., Key, J. R., Casey, K. A., Riggs, G. A., and Cavalieri, D. J.: Sea ice surface temperature product from MODIS, IEEE T. Geosci. Remote, 42, 1076–1087, doi:10.1109/tgrs.2004.825587, 2004.

Hall, D. K., Salomonson, V. V., and Riggs, G. A.: MODIS/Aqua Sea Ice Extent and IST Daily L3 Global 4 km EASE-Grid Day, Version 5, National Snow and Ice Data Center, Boulder, Colorado, USA, 2006.

Hall, D. K., Comiso, J. C., DiGirolamo, N. E., Shuman, C. A., Box, J. E., and Koenig, L. S.: Variability in the surface temperature and melt extent of the Greenland ice sheet from MODIS, Geophys. Res. Lett., 40, 2114–2120, doi:10.1002/grl.50240, 2013.

Hewison, T. J. and English, S. J.: Airborne retrievals of snow and ice surface emissivity at millimeter wavelengths, IEEE T. Geosci. Remote, 37, 1871–1879, doi:10.1109/36.774700, 1999.

Jakob, C.: Cloud cover in the ECMWF reanalysis, J. Climate, 12, 947–959, doi:10.1175/1520-0442(1999)012<0947:cciter>2.0.co;2, 1999.

Jin, M., Dickinson, R. E., and Vogelmann, A. M.: A comparison of CCM2–BATS skin temperature and surface–air temperature with satellite and surface observations, J. Climate, 10, 1505–1524, doi:10.1175/1520-0442(1997)010<1505:ACOCBS>2.0.CO;2, 1997.

Kang, H.-J. and Yoo, J.-M.: Error analysis of three types of satellite-observed surface skin temperatures in the sea ice region of the Northern Hemisphere, J. Korean Earth Sci. Soc., 36, in press, 2015 (in Korean).

Key, J. R., Collins, J. B., Fowler, C., and Stone, R. S.: High-latitude surface temperature estimates from thermal satellite data, Remote Sens. Environ., 61, 302–309, doi:10.1016/S0034-4257(97)89497-7, 1997.

Knuteson, R., Cychosz, J., Lee, S. C., Revercomb, H., Tobin, D., and Vinson, K.: Comparison of LST from AIRS and MODIS from the EOS Aqua platform, 10th symposium on Integrated Observing and Assimilation Systems for the Atmosphere, Oceans, and Land Surface (IOASAOLS), the 86th AMS annual meeting, 2006.

Kongoli, C., Boukabara, S., Yan, B., Weng, F., and Ferraro, R.: Sea ice concentration retrievals from variationally retrieved microwave surface emissivities, available at: http://microrad2008.cetem.org/public/presentations/20080314_16.50_Kongoli.pdf (last access: 4 December 2014), 2008.

Lachlan-Cope, T.: Antarctic clouds, Polar Res., 29, 150–158, doi:10.1111/j.1751-8369.2010.00148.x, 2010.

AMTD
8, 4451–4488, 2015

Lee, Y.-R., Yoo, J.-M., Jeong, M.-J., Won, Y.-I., Hearty, T., and Shin, D.-B.: Comparison between MODIS and AIRS/AMSU satellite-derived surface skin temperatures, Atmos. Meas. Tech., 6, 445–455, doi:10.5194/amt-6-445-2013, 2013.

Li, G., Huang, H.-L., Baggett, K., and Li, J.: Comparison of global AIRS/AMSU and AIRS/MODIS cloud-clearing performance, in: Proc. SPIE 5890, Atmospheric and Environmental Remote Sensing Data Processing and Utilization: Numerical Atmospheric Prediction and Environmental Monitoring, California, USA, 58901D, 2005.

Liou, K. N.: An Introduction to Atmospheric Radiation, Academic Press, Amsterdam, Boston, 2002.

Liu, C. Y., Li, J., Weisz, E., Schmit, T. J., Ackerman, S. A., and Huang, H. L.: Synergistic use of AIRS and MODIS radiance measurements for atmospheric profiling, Geophys. Res. Lett., 35, 6, doi:10.1029/2008gl035859, 2008.

Marshall, J., Armour, K. C., Scott, J. R., Kostov, Y., Hausmann, U., Ferreira, D., Shepherd, T. G., and Bitz, C. M.: The ocean's role in polar climate change: asymmetric Arctic and Antarctic responses to greenhouse gas and ozone forcing, Phil. Trans. R. Soc., 372, 20130040, doi:10.1098/rsta.2013.0040, 2014.

Molnar, G. I. and Susskind, J.: Validation of AIRS/AMSU cloud retrievals using MODIS cloud analyses, in: Proc. SPIE 5806, Algorithms and Technologies for Multispectral, Hyperspectral, and Ultraspectral Imagery XI, 13 July 2005, 618–629, 2005.

Nghiem, S. V., Hall, D. K., Mote, T. L., Tedesco, M., Albert, M. R., Keegan, K., Shuman, C. A., DiGirolamo, N. E., and Neumann, G.: The extreme melt across the Greenland ice sheet in 2012, Geophys. Res. Lett., 39, 6, doi:10.1029/2012gl053611, 2012.

Olsen, E.: AIRS/AMSU/HSB version 6 changes from version 5, available at: http://disc.sci.gsfc.nasa.gov/AIRS/documentation/v6_docs/v6releasedocs-1/V6_Changes_from_V5.pdf (last access: 4 December 2014), 2013a.

Olsen, E.: AIRS/AMSU/HSB version 6 retrieval flow, available at: http://disc.sci.gsfc.nasa.gov/AIRS/documentation/v6_docs/v6releasedocs-1/V6_Retrieval_Flow.pdf (last access: 4 December 2014), 2013b.

Prakash, A.: Thermal remote sensing: concepts, issues and application, XIXth ISPRS Congress, Amsterdam, Netherlands, 239–243, 2000.

Riggs, G. A., Hall, D. K., and Ackerman, S. A.: Sea ice extent and classification mapping with the Moderate resolution Imaging Spectroradiometer airborne simulator, Remote Sens. Environ., 68, 152–163, doi:10.1016/s0034-4257(98)00107-2, 1999.

AMTD
8, 4451–4488, 2015

Riggs, G. A., Hall, D. K., and Salomonson, V. V.: MODIS sea ice products user guide to collection 5, available at: http://modis-snow-ice.gsfc.nasa.gov/uploads/siug_c5.pdf (last access: 7 February 2015), 2006.

Scott, K. A., Li, E., and Wong, A.: Sea ice surface temperature estimation using MODIS and AMSR-E data within a guided variational model along the Labrador Coast, IEEE J. Sel. Top. Appl. Earth Observ. Remote Sens., 7, 3685–3694, doi:10.1109/jstars.2013.2292795, 2014.

Susskind, J., Blaisdell, J. M., Iredell, L., and Keita, F.: Improved temperature sounding and quality control methodology using AIRS/AMSU Data: the AIRS science team version 5 retrieval algorithm, IEEE T. Geosci. Remote, 49, 883–907, doi:10.1109/tgrs.2010.2070508, 2011.

Susskind, J., Blaisdell, J. M., and Iredell, L.: Improved methodology for surface and atmospheric soundings, error estimates, and quality control procedures: the atmospheric infrared sounder science team version-6 retrieval algorithm, APPRES, 8, 084994, doi:10.1117/1.JRS.8.084994, 2014.

Tian, B. J., Fetzer, E. J., Kahn, B. H., Teixeira, J., Manning, E., and Hearty, T.: Evaluating CMIP5 models using AIRS tropospheric air temperature and specific humidity climatology, J. Geophys. Res.-Atmos., 118, 114–134, doi:10.1029/2012jd018607, 2013.

Tobin, D. C., Revercomb, H. E., Knuteson, R. O., Lesht, B. M., Strow, L. L., Hannon, S. E., Feltz, W. F., Moy, L. A., Fetzer, E. J., and Cress, T. S.: Atmospheric radiation measurement site atmospheric state best estimates for atmospheric infrared sounder temperature and water vapor retrieval validation, J. Geophys. Res.-Atmos., 111, 18, doi:10.1029/2005jd006103, 2006.

Wilks, D. S.: Statistical Methods in the Atmospheric Sciences, Academic Press, San Diego, 1995.

Won, Y.-I.: Readme document for AIRS Level-3 version 5 standard products: daily (AIRH3STD, AIRX3STD, AIRS3STD), 8 day (AIRH3ST8, AIRX3ST8, AIRS3ST8) & monthly (AIRH3STM, AIRX3STM, AIRS3STM), available at: http://disc.sci.gsfc.nasa.gov/TRMM/AIRS/documentation/readmes/README.AIR-3ST.pdf (last access: 4 December 2014), 2008.

Yoo, J.-M., Won, Y.-I., Jeong, M.-J., Kim, K.-M., Shin, D.-B., Lee, Y.-R., and Cho, Y.-J.: Intensity of climate variability derived from the satellite and MERRA reanalysis temperatures: AO, ENSO, and QBO, J. Atmos. Sol.-Terr. Phys., 95–96, 15–27, doi:10.1016/j.jastp.2013.01.002, 2013.

AMTD
8, 4451–4488, 2015

Table 1. The information on the satellite-observed surface skin temperature (T_{skin}) Level 3 (L3) data used in this study. Three datasets of T_{skin} were compared over the Northern Hemisphere during 16–24 April of 2003–2014, and over the Southern Hemisphere during 15–23 September of 2003–2014. The abbreviations used in this table are as follows: temp (temperature), IST (ice surface skin temperature), OBS (observation), and SFC (surface).

Satellite-observed dataset	Version (Collection)	Temp type	Area	Spatial resolution	Number of OBS	Satellite sensor	Abbreviation	Reference
MODIS IST	MYD29E1D/5	Skin	Polar ocean	4 km × 4 km	1 day^{-1}	Aqua MODIS	T_{skin} (MODIS)	Hall et al. (2004)
AIRS/AMSU SFC skin temp	AIRX3STD/6	Skin	Globe	1° × 1°	2 day^{-1}	Aqua AIRS/AMSU-A	T_{skin} (AA_V6)	Susskind et al. (2014)
AIRS Only SFC skin temp	AIRS3STD/6	Skin	Globe	1° × 1°	2 day^{-1}	Aqua AIRS	T_{skin} (AO_V6)	Susskind et al. (2014)

AMTD
8, 4451–4488, 2015

Table 2. Statistical comparisons of the climatological 9 day composite data during 2003–2014 over both hemispheres; T_{skin} (MODIS) vs. T_{skin} (AA_V6), T_{skin} (MODIS) vs. T_{skin} (AO_V6), and T_{skin} (AO_V6) vs. T_{skin} (AA_V6). The values in this table were calculated based on the 12 year composite mean values. The values in parentheses indicate the 12 year mean values and their SDs during 2003–2014. Bias: T_{skin} (MODIS) minus T_{skin} (AA_V6), T_{skin} (MODIS) minus T_{skin} (AO_V6), and T_{skin} (AO_V6) minus T_{skin} (AA_V6), r: correlation coefficient, RMSE: root mean square error.

Region	T_{skin} (MODIS) vs. T_{skin} (AA_V6)			T_{skin} (MODIS) vs. T_{skin} (AO_V6)			T_{skin} (AO_V6) vs. T_{skin} (AA_V6)		
	Bias (K)	r	RMSE (K)	Bias (K)	r	RMSE (K)	Bias (K)	r	RMSE (K)
35–90° N	−0.169	0.994	1.491	−0.289	0.993	1.563	0.133	0.999	0.574
	(−0.161 ± 0.231)	(0.990 ± 0.002)	(1.909 ± 0.156)	(−0.324 ± 0.308)	(0.990 ± 0.003)	(1.963 ± 0.260)	(0.137 ± 0.130)	(0.997 ± 0.001)	(1.018 ± 0.131)
40–90° S	0.026	0.989	1.480	0.203	0.985	1.756	−0.14	0.998	0.750
	(−0.010 ± 0.218)	(0.982 ± 0.003)	(2.082 ± 0.144)	(0.035 ± 0.282)	(0.980 ± 0.003)	(2.184 ± 0.119)	(−0.139 ± 0.079)	(0.994 ± 0.001)	(1.272 ± 0.092)
60–90° N	0.223	0.986	1.501	0.597	0.986	1.591	0.168	0.998	0.590
	(0.194 ± 0.357)	(0.973 ± 0.009)	(1.986 ± 0.227)	(−0.013 ± 0.475)	(0.972 ± 0.011)	(2.033 ± 0.370)	(0.170 ± 0.214)	(0.992 ± 0.003)	(1.027 ± 0.216)
60–90° S	0.198	0.968	1.847	0.306	0.959	2.173	−0.109	0.992	0.852
	(0.368 ± 0.537)	(0.906 ± 0.023)	(2.871 ± 0.276)	(0.295 ± 0.620)	(0.898 ± 0.021)	(2.987 ± 0.271)	(−0.108 ± 0.142)	(0.976 ± 0.005)	(1.498 ± 0.112)

AMTD
8, 4451–4488, 2015

Table 3. The rate of the surface skin temperature change (K decade^{-1}) of the MODIS, AIRS/AMSU, and AIRS only in each 10° latitudinal belt over the Northern Hemisphere (NH) during 16–24 April and over the Southern Hemisphere (SH) during 15–23 September of 2003–2014, using their collocated data in a 1° × 1° grid. The ± values define the 95 % confidence intervals for the trends. The symbol "∗" means the significant value at a 95 % confidence interval. Note that the rates are subject to large uncertainty due to the short periods of the satellite-based temperature records.

Latitudinal belt	MODIS	AIRS/AMSU	AIRS only	MODIS minus AIRS/AMSU	MODIS minus AIRS only	AIRS only minus AIRS/AMSU
⟨NH⟩						
80–90° N	−0.558 ± 3.101	−0.100 ± 3.673	−0.093 ± 3.736	−0.458	−0.465	0.007
70–80° N	2.302 ± 1.701*	2.826 ± 1.878*	2.711 ± 1.788*	−0.524	−0.409	−0.115
60–70° N	−0.506 ± 1.173	−0.646 ± 1.294	−0.902 ± 1.050	0.140	0.396	−0.256
50–60° N	−0.345 ± 0.539	−0.522 ± 0.628	−0.466 ± 0.550	0.177	0.121	0.056
40–50° N	0.292 ± 0.402	0.103 ± 0.576	0.191 ± 0.565	0.189	0.101	0.088
⟨SH⟩						
50–60° S	0.375 ± 0.400	0.315 ± 0.466	0.316 ± 0.600	0.060	0.059	0.001
60–70° S	−1.944 ± 2.271	−1.304 ± 1.890	−1.300 ± 1.918	−0.640	−0.644	0.004
70–80° S	−0.769 ± 2.687	−0.081 ± 2.586	−0.135 ± 2.633	−0.688	−0.634	−0.054

AMTD
8, 4451–4488, 2015

Table 4. Uncertainties of the satellite-derived surface skin temperature rate (or trend; ΔTrend) due to the temperature difference (ΔT_{skin}) for the cases of T_{skin} (MODIS) minus T_{skin} (AA_V6) and T_{skin} (AO_V6) minus T_{skin} (AA_V6) in the upper portion of the table. Also, the values of uncertainties provided in the lower portion of the table indicate the cases of ±ΔTrend with respect to ±ΔT_{skin} (double signs in the same order). The uncertainties are not shown when the number of the grid (1° × 1°) points (i.e., No. of grids in the table) is less than 100.

ΔT_{skin} (K)	Poleward from 50° N						Poleward from 50° S					
	T_{skin} (MODIS) vs. T_{skin} (AA_V6)			T_{skin} (AO_V6) vs. T_{skin} (AA_V6)			T_{skin} (MODIS) vs. T_{skin} (AA_V6)			T_{skin} (AO_V6) vs. T_{skin} (AA_V6)		
	No. of grids	ΔT_{skin}	ΔTrend (K decade^{-1})	No. of grids	ΔT_{skin}	ΔTrend (K decade^{-1})	No. of grids	ΔT_{skin}	ΔTrend (K decade^{-1})	No. of grids	ΔT_{skin}	ΔTrend (K decade^{-1})
≥ 1.0	2155	2.01	−0.10	95	–	-	425	2.01	−0.96	378	1.37	0.03
≥ 1.5	1506	2.34	0.04	19	–	-	253	2.25	−0.66	104	1.80	0.24
≥ 2.0	940	2.71	0.19	5	–	-	134	2.69	−0.21	22	–	–
≤ −1.0	1839	−1.59	−0.45	236	−2.25	−0.34	224	−1.71	−0.43	877	−2.19	−0.37
≤ −1.5	921	−1.94	−0.45	162	−2.72	−0.47	115	−2.18	−0.16	654	−2.52	−0.55
≤ −2.0	367	−2.27	−0.60	109	−3.20	−0.78	55	–	-	472	−2.82	−0.69
≥ 1.0	912	2.15	1.21	40	–	-	139	2.09	1.36	179	1.40	1.01
≥ 1.5	707	2.41	1.22	8	–	-	94	–	-	51	–	–
≥ 2.0	499	2.70	1.22	1	–	-	64	–	-	15	–	–
≤ −1.0	1309	−1.59	−0.90	126	−2.51	−2.02	122	−1.69	−2.42	500	−2.26	−1.96
≤ −1.5	643	−1.96	−0.92	89	–	-	61	–	-	387	−2.55	−2.06
≤ −2.0	272	−2.28	−1.02	69	–	-	27	–	–	293	−2.81	−2.06

AMTD
8, 4451–4488, 2015

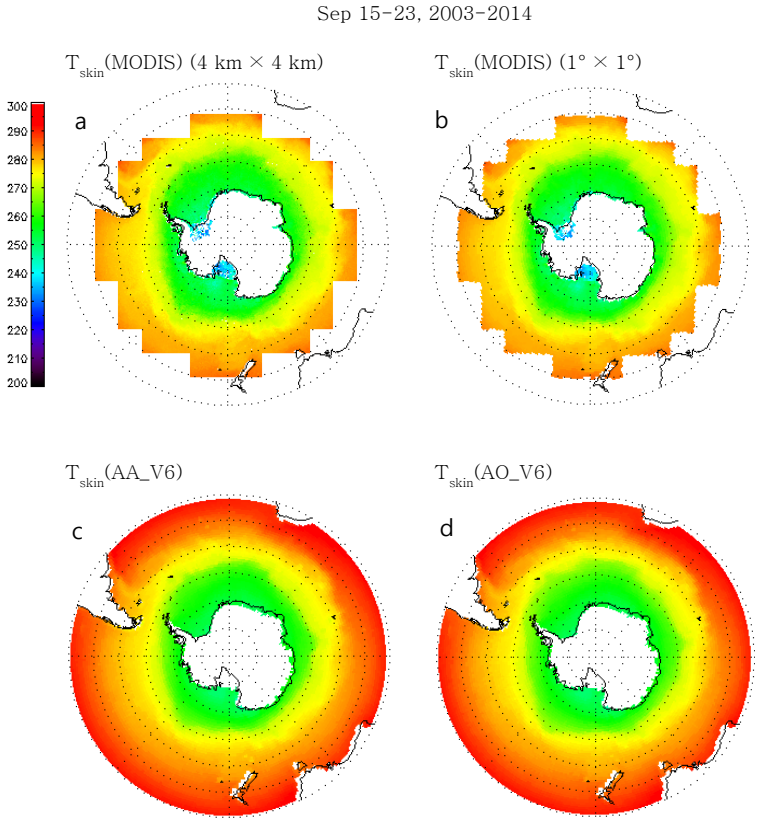

Figure 1. (a) 12 year composite skin temperatures (K) of the MODIS IST over the Southern Hemisphere during 15–23 September of 2003–2014. The original MODIS data (MYD29E1D) have a 4 km × 4 km spatial resolution. Their spatial resolution has been reconstructed to 1° × 1° in **(b)** in order to compare this data with the AIRS/AMSU data. **(c** and **d)** are the surface skin temperatures of the AIRS/AMSU and AIRS only over the Southern Hemisphere ocean during 15–23 September of 2003–2014, respectively.

AMTD
8, 4451–4488, 2015

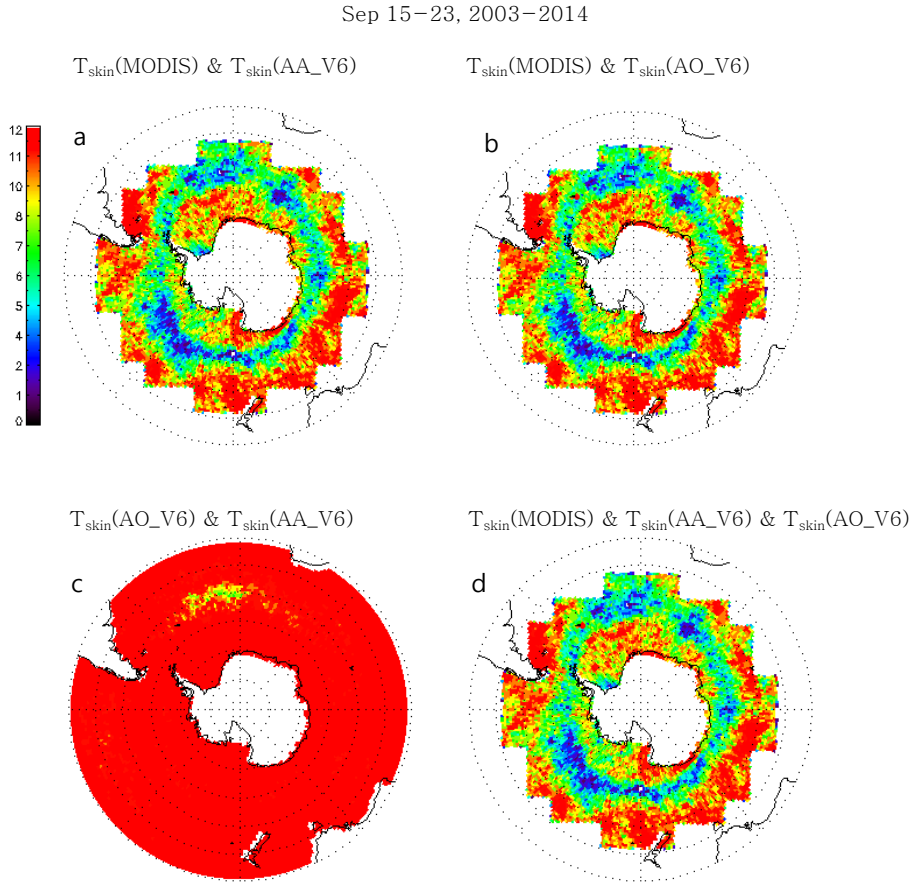

Figure 2. The number of co-located observations of **(a)** T_{skin} (MODIS) and T_{skin} (AA_V6), **(b)** T_{skin} (MODIS) and T_{skin} (AO_V6), and **(c)** T_{skin} (AO_V6) and T_{skin} (AA_V6) over the Southern Hemisphere during 15–23 September of 2003–2014. **(d)** Same as in **(c)** except for three different datasets (T_{skin} (MODIS), T_{skin} (AA_V6), and T_{skin} (AO_V6)).

AMTD
8, 4451–4488, 2015

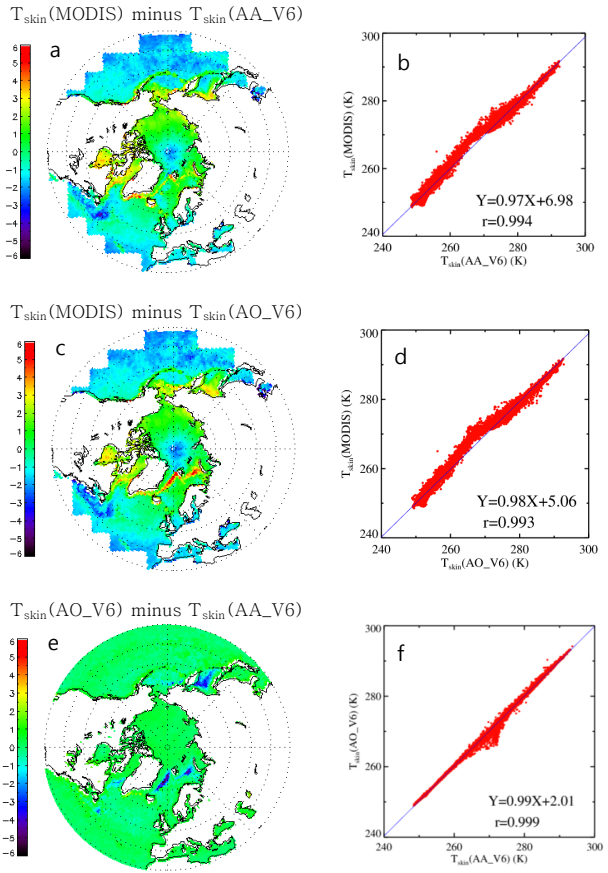

Figure 3. The distributions of **(a)** T_{skin} (MODIS) minus T_{skin} (AA_V6), **(c)** T_{skin} (MODIS) minus T_{skin} (AO_V6), and **(e)** T_{skin} (AO_V6) minus T_{skin} (AA_V6) over the Northern Hemisphere during 16–24 April of 2003–2014. The scatter plots of **(b)** T_{skin} (MODIS) vs. T_{skin} (AA_V6), **(d)** T_{skin} (MODIS) vs. T_{skin} (AO_V6), and **(f)** T_{skin} (AO_V6) vs. T_{skin} (AA_V6).

AMTD
8, 4451–4488, 2015

Uncertainties of satellite-derived surface skin temperatures in the polar oceans

H.-J. Kang et al.

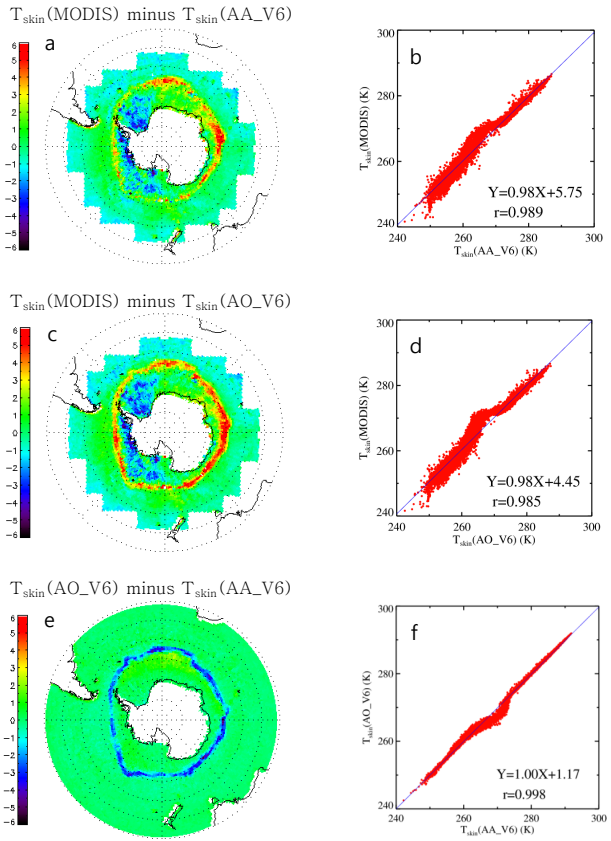

Figure 4. Same as in Fig. 3 except for the data taken during 15–23 September of 2003–2014, over the Southern Hemisphere.

AMTD
8, 4451–4488, 2015

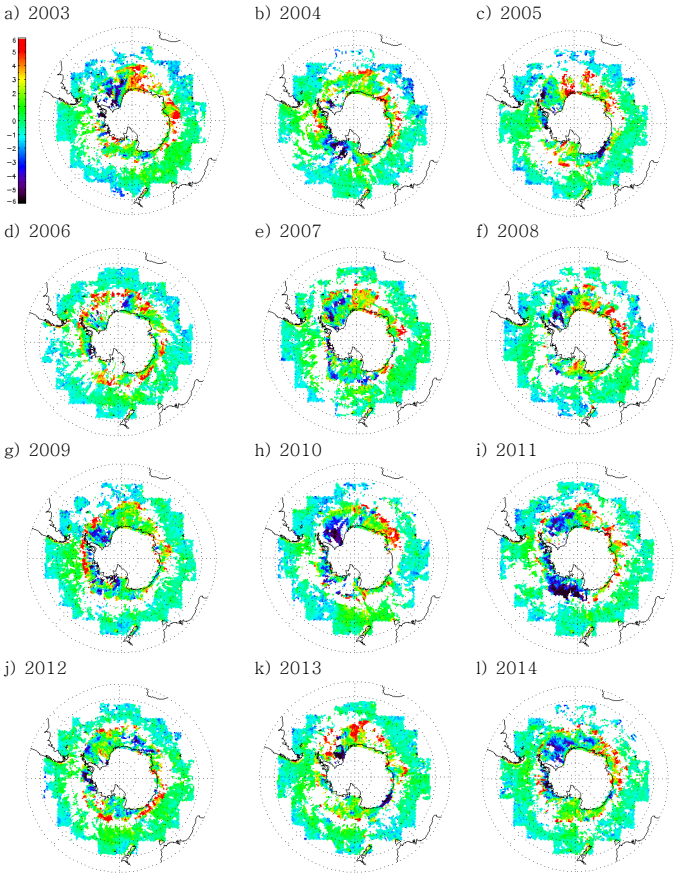

Figure 5. Interannual variations of the T_{skin} (MODIS) minus T_{skin} (AA_V6) over the Southern Hemisphere during 15–23 September.

AMTD
8, 4451–4488, 2015

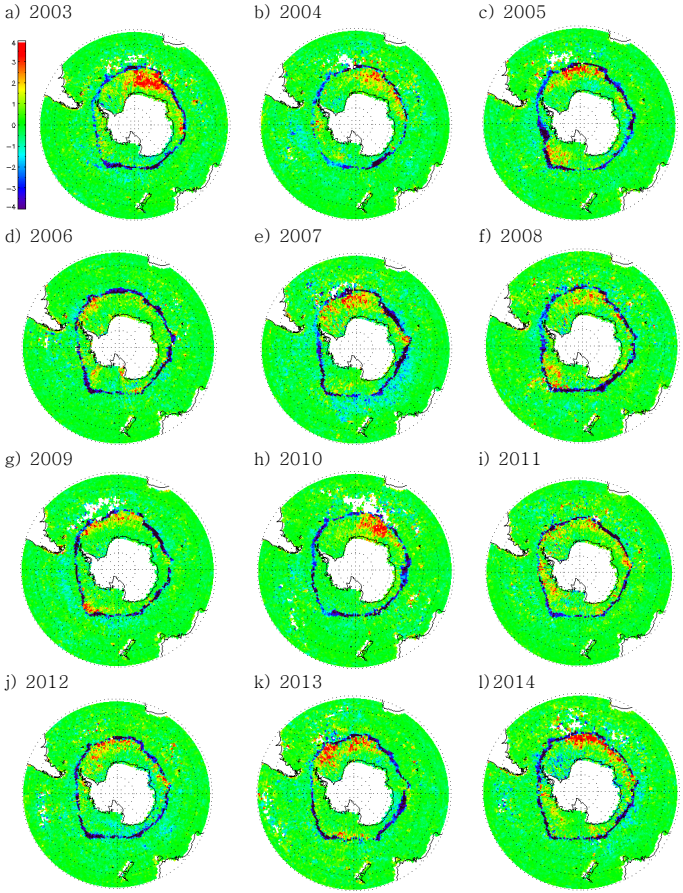

Figure 6. Same as Fig. 5 except for T_{skin} (AO_V6) minus T_{skin} (AA_V6).

AMTD
8, 4451–4488, 2015

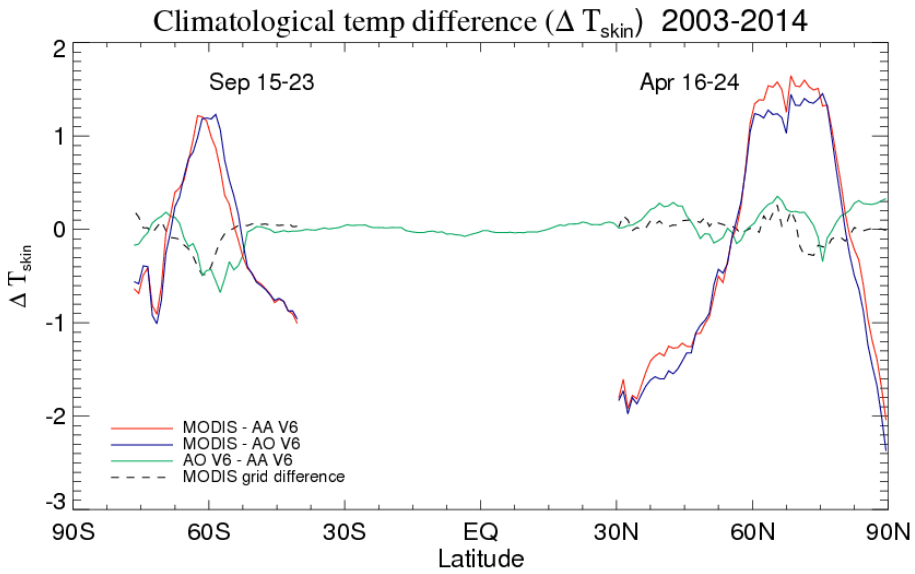

Figure 7. Zonal averaged values of T_{skin} (MODIS) minus T_{skin} (AA_V6) (red solid line), T_{skin} (MODIS) minus T_{skin} (AO_V6) (blue solid line), and T_{skin} (AO_V6) minus T_{skin} (AA_V6) (green solid line). The difference in spatial grid averages of the MODIS data between 4 km by 4 km and 1° by 1° is shown by the black dashed line. The difference values are calculated at one degree interval along each latitudinal belt. The climatological data periods are 16–24 April 2003–2014 over the Northern Hemisphere, and 15–23 September 2003–2014 over the Southern Hemisphere.

AMTD
8, 4451–4488, 2015

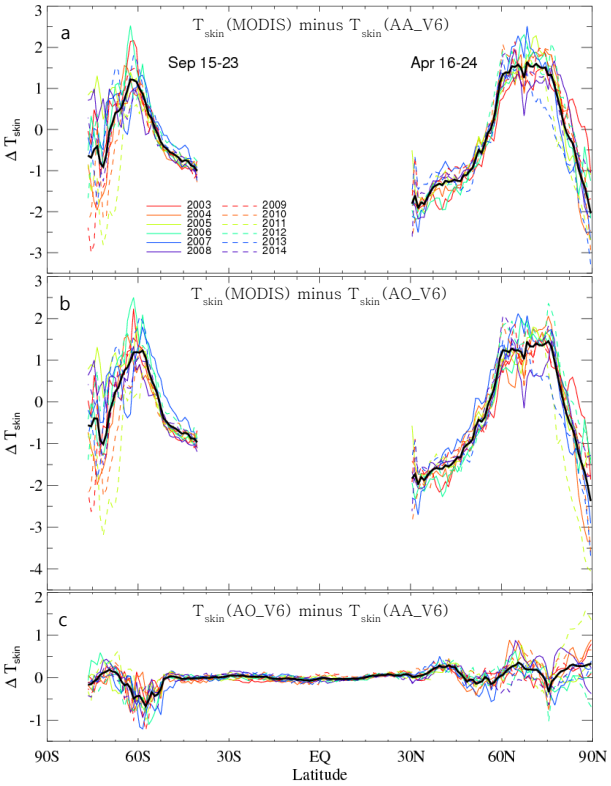

Figure 8. Zonal averaged values of **(a)** T_{skin} (MODIS) minus T_{skin} (AA_V6), **(b)** T_{skin} (MODIS) minus T_{skin} (AO_V6), **(c)** T_{skin} (AO_V6) minus T_{skin} (AA_V6) over the Northern Hemisphere from 16 to 24 April 2003–2014, and over the Southern Hemisphere from 15 to 23 September 2003–2014. The values in each year represent the corresponding color lines. The thick black line indicates the mean difference values.

AMTD
8, 4451–4488, 2015

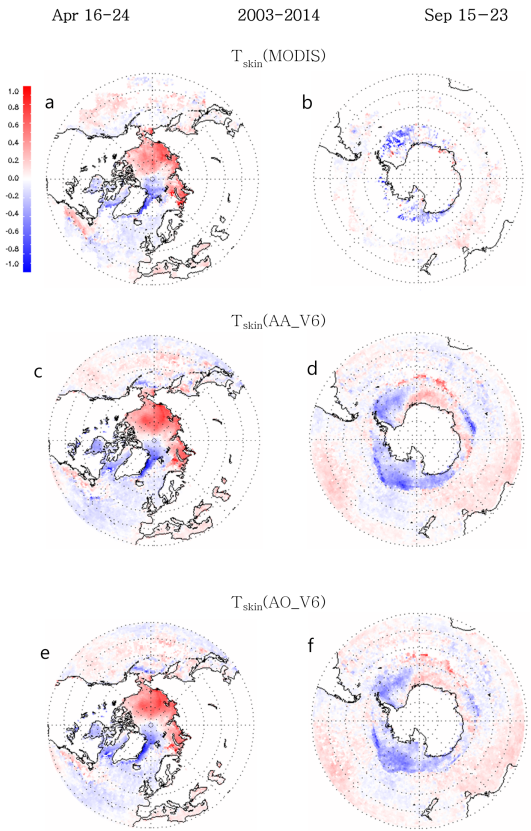

Figure 9. Satellite-derived 9 day anomaly trends ($K\,yr^{-1}$) in a grid box of $1^\circ \times 1^\circ$ over the Northern Hemisphere during 16–24 April of 2003–2014, for the **(a)** T_{skin} (MODIS), **(c)** T_{skin} (AA_V6), and **(e)** T_{skin} (AO_V6), and over the Southern Hemisphere during 16–24 September of 2003–2014, for the **(b)** T_{skin} (MODIS), **(d)** T_{skin} (AA_V6), and **(f)** T_{skin} (AO_V6).

AMTD
8, 4451–4488, 2015

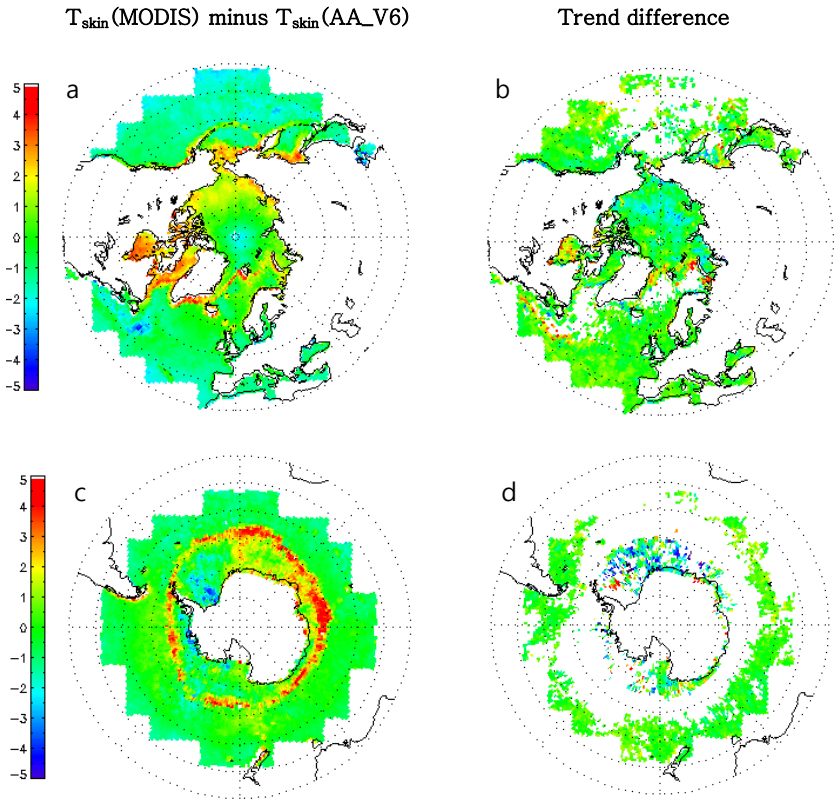

Figure 10. (a) 12 year mean of T_{skin} (MODIS) minus T_{skin} (AA_V6) (K) over the Northern Hemisphere during 16–24 April of 2003–2014, and **(b)** difference in the thermal trend (K decade^{-1}) between T_{skin} (MODIS) and T_{skin} (AA_V6). **(c** and **d)** are the same as **(a** and **b)** except for over the Southern Hemisphere during 16–24 September of 2003–2014, respectively. **(a)** is the same as Fig. 3a in Kang and Yoo (2015).

AMTD
8, 4451–4488, 2015

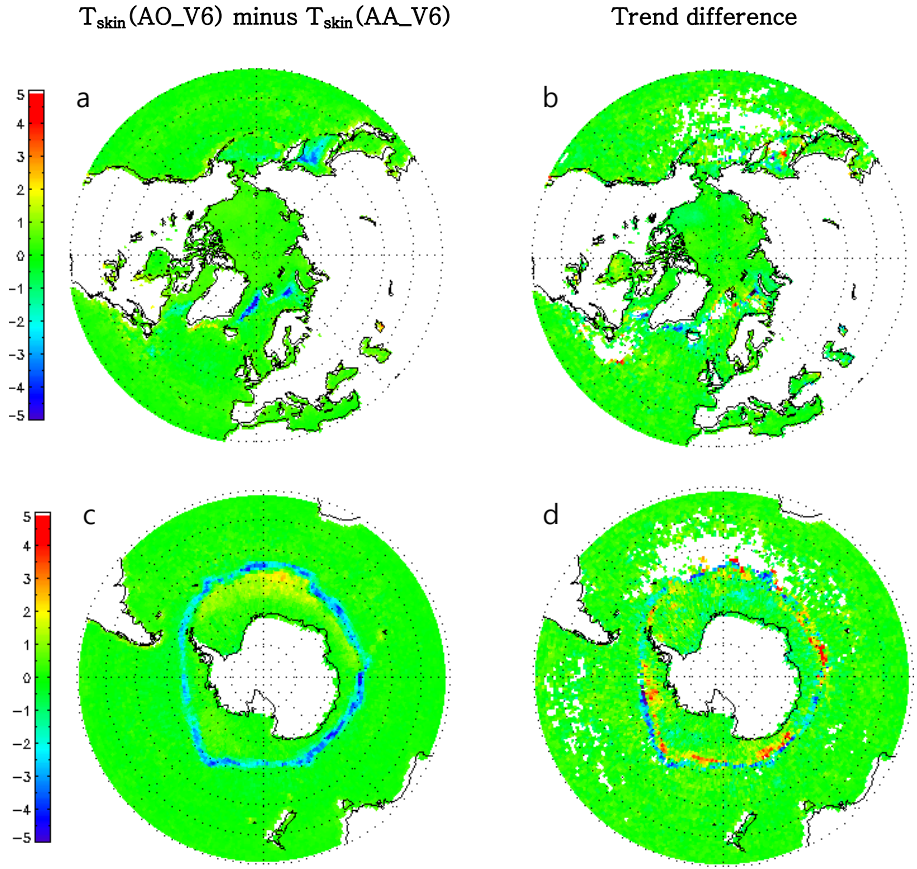

Figure 11. Same as Fig. 10 except for T_{skin} (AO_V6) minus T_{skin} (AA_V6). **(a)** is the same as Fig. 3c in Kang and Yoo (2015).

AMTD
8, 4451–4488, 2015

Uncertainties of satellite-derived surface skin temperatures in the polar oceans

H.-J. Kang et al.